J Nanopart Res (2022) 24:214
https://doi.org/10.1007/s11051-022-05596-z

RESEARCH PAPER

Dependence of specific absorption rate on concentration of Fe_3O_4 nanoparticles: from the prediction of Monte Carlo simulations to experimental results

Le Tri Dat · Luu Huu Nguyen · Nguyen Hoai Nam · Tuan Dinh Van · Le The Tam · Nguyen Xuan Truong · Van-Quynh Nguyen · Pham Thanh Phong · Pham Hong Nam

Received: 6 June 2022 / Accepted: 12 October 2022

Abstract Specific absorption rate (SAR) of magnetic iron oxide (Fe_3O_4) nanoparticles (NPs) is an important property in hyperthermia applications. In this work, the dependence of magnetic anisotropy (K) on concentration of Fe_3O_4 NPs has been investigated using the Monte Carlo simulations. The results showed that the K value increases with the NPs concentration which helps to clarify the dual behavior of both increase and decrease of SAR value with concentration based on the Linear Response Theory (LRT). The theoretical results explained the influence of concentration on SAR based on the relationship between magnetic anisotropy and inter-particle distance. Furthermore, Fe_3O_4 NPs of size range from 7 to 17 nm have been synthesized with high magnetization saturation (65.1–68.1 emu/g) and their superparamagnetic behaviors have been determined. The experimental results indicated that the SAR value could increase with the concentration and has a bell shape at a specific size of MNPs, which are in good agreement with the theoretical simulation. All theoretical and experimental study of SAR recognized the important role of magnetic anisotropy to enhance SAR values. Especially, the results showed that there exists an optimal concentration at 15 mg/ml for 17 nm Fe_3O_4 NPs that maximized SAR value.

L. T. Dat (✉)
Computational Laboratory for Advanced Materials and Structures, Advanced Institute of Materials Science, Ton Duc Thang University, Ho Chi Minh City, Vietnam
e-mail: letridat@tdtu.edu.vn

L. T. Dat
Faculty of Applied Sciences, Ton Duc Thang University, Ho Chi Minh City, Vietnam

L. H. Nguyen (✉) · P. T. Phong
Laboratory of Magnetism and Magnetic Materials, Science and Technology Advanced Institute, Van Lang University, Ho Chi Minh City, Vietnam
e-mail: luuhuunguyen@vlu.edu.vn

L. H. Nguyen · P. T. Phong
Faculty of Applied Technology, School of Engineering and Technology, Van Lang University, Ho Chi Minh City, Vietnam

N. H. Nam · N. X. Truong · P. H. Nam
Institute of Materials Science, Vietnam, Academy of Science and Technology, 18 Hoang Quoc Viet, Cau Giay, Hanoi, Vietnam

T. D. Van
Electric Power University, 235 Hoang Quoc Viet, Bac Tu Liem, Hanoi, Vietnam

L. T. Tam
Vinh University, 182 Le Duan, Vinh, Vietnam

V.-Q. Nguyen
University of Science and Technology of Hanoi (USTH), Vietnam, Academy of Science and Technology, 18 Hoang Quoc Viet, Cau Giay, Hanoi, Vietnam

P. H. Nam
Graduate University of Science and Technology, Vietnam, Academy of Science and Technology, 18 Hoang Quoc Viet, Cau Giay, Hanoi, Vietnam

Published online: 21 October 2022

Keywords Monte Carlo simulation · Concentration · Specific absorption rate · Magnetic anisotropy · Inter-particle interactions

Introduction

Magnetic nanoparticles (MNPs) have been used for biomedical applications, especially in cancer therapy based on magnetic inductive heating (MIH) [1, 2]. To date, there are a lot of works showing a high specific absorption rate (SAR), or high specific loss power (SLP) of MNPs has an impact on the ability of the removal of cancer cells as well as decreasing the number of MNPs [2, 3]. Among MNPs, magnetite (Fe_3O_4) has attracted increasing attention because of its biocompatibility, high saturation, chemical stability, and simple fabrication methods [2]. Unfortunately, there is a strong decrease in the saturation magnetization of Fe_3O_4 MNPs upon size reduction in nanoscale, which leads to a decrease in SAR value. For example, the SAR value of Fe_3O_4 MNPs with size in the range of biomedical application (10–20 nm) was much lower than that of the particles in the 30–40-nm range [4]. Therefore, its concentration (the number of MNPs in fluids) must be high in order to enhance SAR, but this can be toxic to healthy cells and limit their application in MIH [3]. So, the relationship between the concentration and the SAR value of Fe_3O_4 MNPs needs to be systematically considered.

Nowadays, researchers have taken advantage of the development of the computational tool to carry out numerical studies about the physical phenomena of MNPs by using theoretical calculations and simulations. For example, in MIH, Rosensweig used Linear Response Theory (LRT) to calculate the heating efficiency of magnetic fluids [5]. Hergt et al. [6] and Carrey et al. [7] studied MIH of MNPs by Stoner–Wohlfarth model-based theories (SWMBTs). In addition, Papadopoulos et al. [8], Eddahri et al. [9], Kanaoujiya et al. [10], and Wu et al. [11] studied MIH of MNPs by a technique simulation, the so-called Monte Carlo (MC) simulation. This technique simulation was introduced for first time in the work of Binder et al. in 1970 [12]. Subsequently, Binder et al. demonstrated a good qualitative agreement between the predictions of this simulation and the trend of experimental results [13]. Therefore, until now, the MC method based on Metropolis Algorithm [14] remains the most one [15] for numerical studies.

In order to investigate the dependence of SAR on the concentration, Tan et al. used MC simulations [16]. The interesting results of the work of Tan et al. were the increase, decrease, or bell shape of the plot of SAR versus concentration [16]. These contradictory trends were also observed in other works. For instance, Urtizberea et al. [17] and De la Presa et al. [18] revealed a decrease in the SAR value while the concentration of MNPs increased. The stronger inter-particle interactions with shorter inter-particle distance were used explain to this tendency. However, this hypothesis might not be consistent with other tendencies. In contrast to these above results, Maternez-Boubeta et al. found a slight increase of SAR with a growing in the concentration [19]. In addition, the existence of optimal concentration of MNPs was found in a work of Haase et al. [20]. In an interesting work by Kim et al., a decrease of SLP with an increase of the concentration in a range of 0.1 to 0.5 mg/ml was discovered at H = 70–140 Oe; however, there is also an existence of an optimal concentration in a range of 1 to 100 mg/ml at 140 Oe [21]. Although the impact of the concentration of MNPs on the SAR value was confirmed in the above works, these contradictory trends cannot be explained by theories such as LRT and SWMBTs because the theoretical SAR cannot be dependent on the concentration [5, 22]. This is still an interesting topic that needs attention.

Recently, the results of these works of Lan et al. [23], Nemati et al. [24], Carrey et al. [7], and Habib et al. [25] have provided a new approach to explain this problem. The work of Lan et al. found that the blocking temperature shifted rapidly toward higher temperatures with an increase of the concentration by MC simulations [23]. This result found the relation between the magnetic anisotropy (K) and the concentration of MNPs. In addition, the works of Nemati et al. [24], Carrey et al. [7], and Habib et al. [25] found that the SAR value can either increase or decrease when the K value increased. Thus, the dependence of SAR on the concentration of MNPs can be systematically explained based on the relations between K and SAR, and the K value and the concentrations.

As mentioned above, these above relationships have suggested a new approach to find the mechanism of the dependence SAR on the concentration. In order to find this mechanism, we applied MC simulations to create a model for investigating the effect of inter-particle distance ($d_{c\text{-}c}$) on the K value of MNPs. The results of MC simulations confirmed the dependence of the K value on the $d_{c\text{-}c}$ value, relating to the concentration of MNPs in fluids. Based on this prediction of MC simulations, the relationship between the theoretical SAR value and the K value for 7, 11, and 17 nm Fe_3O_4 MNPs was calculated by LRT. The theoretical results found the existence of a peak of the plots SAR (K) for 11-nm and 17-nm Fe_3O_4 MNPs. Corresponding to these theoretical trends, there exist optimal concentrations for the above MNPs. Next, for comparison of the theoretical tendency with experimental data, we have prepared Fe_3O_4 MNPs by the co-precipitation method. All samples had average size in a range of 7–17 nm with narrow distribution and superparamagnetic behavior. All results demonstrated that the experimental tendency of the dependence of SAR on the concentration was in good agreement with the predictions of theoretical ones. Especially, there was an optimal concentration for 17-nm Fe_3O_4 MNPs in practice.

Model and theoretical results

Model

To investigate the dependence of K value on the concentration of MNPs in fluids, we built the model based on the relationship between the inter-particle distance $d_{c\text{-}c}$ and the inter-particle interactions (Fig. 1). Hence, the energy of each MNPs with the presence of the dipolar interaction would be [23, 26]

$$E^{(i)} = -K_u V_i \left(\frac{\boldsymbol{\mu}_i \cdot \boldsymbol{n}_i}{|\boldsymbol{\mu}_i|} \right) - \boldsymbol{\mu}_i \boldsymbol{H} + g \sum_{j \neq i}^{N} \left(\frac{\boldsymbol{\mu}_i \cdot \boldsymbol{\mu}_j}{r_{ij}^3} - 3 \frac{(\boldsymbol{\mu}_i \cdot \boldsymbol{r}_{ij})(\boldsymbol{\mu}_j \cdot \boldsymbol{r}_{ij})}{r_{ij}^5} \right) \quad (1)$$

In Eq. (1), the first term is the anisotropy energy, and $\boldsymbol{n}_i$ is the direction of the anisotropy axis with $|\boldsymbol{n}_i| = 1$. The second and third terms are Zeeman energy and the energy of inter-particle interactions (dipolar interactions) between two MNPs i and j separated by $\boldsymbol{r}_{ij}$, with $\boldsymbol{H}$ as the external field and constant $g = {}^{\mu_0}/_{4\pi}$ with μ_0 as the vacuum permeability. The shortest value of $\boldsymbol{r}_{ij}$ is the value of $d_{c\text{-}c}$. An equilibrium configuration meant minimization of the energy can be obtained using the MC method. In our work, an initial configuration generated 512 particles with (8, 8, 8) size. Each nanoparticle had its total magnetic moment, $|\boldsymbol{\mu}_i| = M_S V_i$, with random values (θ, φ) with $\theta \in [0, 2\pi]$, and $\varphi \in [0, 2\pi]$, and a volume that can be obtained from a lognormal distribution, $g(D)$:

$$g(D) = \frac{1}{\sqrt{2\pi}\sigma D} \exp\left(\frac{-\left(\ln\left(\frac{D}{D_0}\right)\right)^2}{2\sigma^2} \right) \quad (2)$$

where D_0 and σ are the mean size (diameter) and standard deviation (size dispersion), respectively.

The external field $\boldsymbol{H}$ was assumed along the z-axis direction. Besides, we believed that all directions of the easy axis of MNPs aligned at an angle Ψ with the field and a magnetization orientated. So as to optimize this configuration, a procedure was written as follows: (1) a position in the configuration was randomly chosen and the angle values (θ, φ) from that position is extracted; (2) a new orientation was created by the expression $(\theta + \delta, \varphi + \delta)$ where δ is a small value and selected

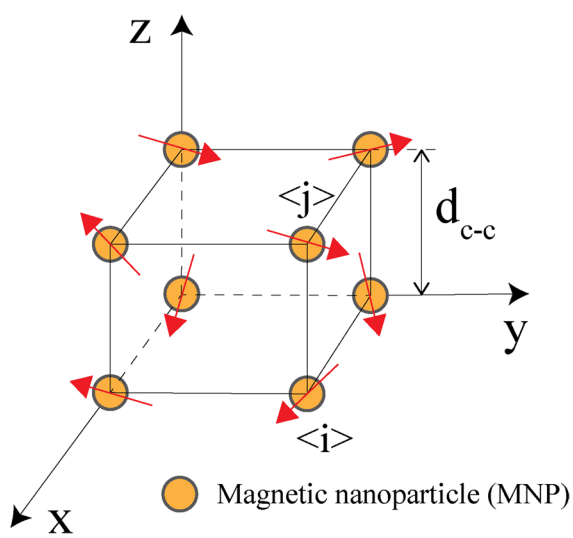

Fig. 1 The schematic of MNPs with the shortest inter-particle distance, $d_{c\text{-}c}$

randomly from − 1 to 1; (3) both energies of current E_{curr} and new angles E_{new} were calculated; (4) the difference of energy, $\Delta E = E_{new} - E_{curr}$, was also computed; (5) the new orientation can be updated to the configuration with a probability min $\left[1, \exp(-\Delta E/k_T B)\right]$.

In order to describe the relationship between SAR value and the concentration of MNPs in fluids, we applied the Linear Response Theory (LRT) to calculate the theoretical SAR value, SAR_{theo}. We note that the LRT is suitable for superparamagnetic nanoparticles [7]. Based on LRT, the value of SAR_{theo} (W/g) can be determined as follows [22]:

$$\boldsymbol{SAR_{theo} = \frac{P}{\phi\rho}} \tag{3}$$

where ϕ is the fraction of volume, ρ is the mean mass density of MNPs, and P is loss power of MNPs. Based on the LRT, the P value can be expressed [22]:

$$\boldsymbol{P = \pi\mu_0\chi_0 H^2 f \frac{2\pi f^2 \tau}{1 + (2\pi f\tau)^2}} \tag{4}$$

where μ_0 is the permeability of free space, H is the amplitude of alternating magnetic fields (AMF), f is the frequency of AMF, χ_0 is the initial dc susceptibility, and τ is the relation time as shown in detail in [22, 27].

Theoretical results

In order to compare theoretical results with experimental ones, we used experimental data to build the model for Fe_3O_4 MNPs. Following the mentioned model, we initially investigated the zero-field cool (ZFC) curves for 7, 11, and 17 nm Fe_3O_4 MNPs (mentioned in the "Experimental results and discussion" section) corresponding to S1, S2, and S3 samples, respectively. For one thing, we evaluated the influence of the concentration of MNPs in fluid on the ZFC peak related to the value of blocking temperature, T_B. From there, we relied on the proportional relationship between (anisotropy energy) KV and (thermal energy) $k_b T_B$ to evaluate the effect of the concentration on the value of K for each sample. For another thing, we assumed that when the concentration of MNPs in fluid increased, the state of the sample changed from dilute to solid (from "weak" interaction to strong interaction between Fe_3O_4 MNPs), and the magnetic anisotropy of each sample might increase approach the value of K of dried samples mentioned in the "Experimental results and discussion" section. Finally, we quantified the reduction of K by the concentration of MNPs for each sample.

Figure 2 represents ZFC curves of all dilute S1, S2, and S3 samples. As can be seen in Fig. 2, each ZFC hit a peak where the temperature was the blocking temperature, T_B. Garcia-Otero et al. expressed that the value of T_B was not dependent on the sample's dispersion [28]; however, all results indicated that there was a shift to higher temperature of T_B when the size distribution changed from monodispersity to polydispersity (as represented in Fig. 5). For S1 sample, T_B value change from 22.5 K (monodispersity) to 26.5 K at $\sigma = 0.1$, and 29.5 K at $\sigma = 0.2$. Similarly, T_B value changed from 339.5 K (monodispersity) to 364.5 K at $\sigma = 0.1$, and 657.5 K at $\sigma = 0.2$ for S3 sample. For S2 sample, T_B value changed from 90.5 K (monodispersity) to 96.5 K at $\sigma = 0.1$. Except for the case at $\sigma = 0.2$ of S2 sample, it is clear that the T_B value of each sample at $\sigma \neq 0$ (polydispersity) is higher than that of one at $\sigma = 0$ (monodispersity). This tendency is in good agreement with those reported earlier [23]. Lan et al. found that there was a shift to higher temperature of T_B value for 7.5 nm γ-Fe_2O_3 [23]. Despite the shift to higher temperature of T_B when the size distribution changed from monodispersity to polydispersity for S2 sample, the value of T_B at $\sigma = 0.1$ was higher than the ones at $\sigma = 0.2$. This result showed that the influence of dispersion on the T_B value was complex because of the contribution of MNPs with various sizes when distribution was widened. Thus, it should be taken into account the size distribution in investigating the influence of the concentration (linked to $d_{c\text{-}c}$) on the T_B value.

For each sample, we used the above model to determine the value of T_B in ZFC curve with the various value of $d_{c\text{-}c}$. Then, we investigated the influence of T_B on $d_{c\text{-}c}$. The summary of the results is described in Fig. 3. Based on a simple inter-particle interactions model, we fitted these outcomes under the following theoretical formula [26]:

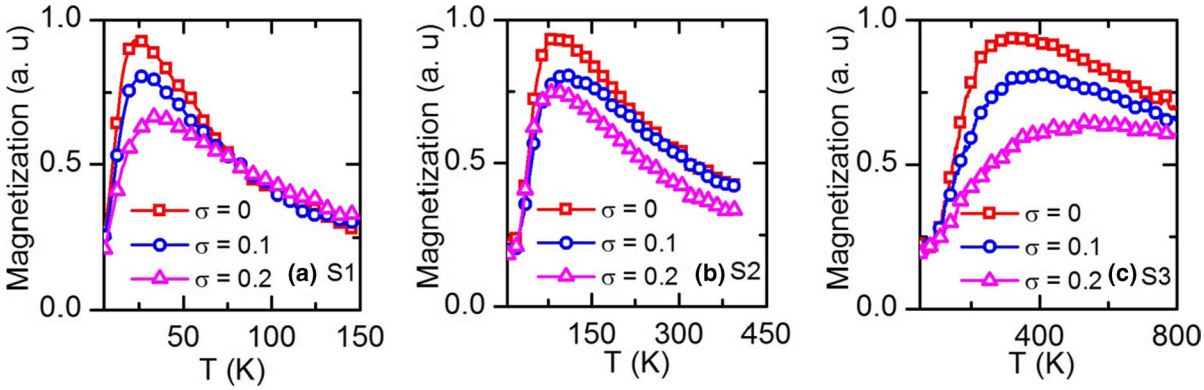

Fig. 2 ZFC curves at various value of σ for **a** S1, **b** S2, and **c** S3 samples

$$\frac{T_B}{T_0} = A + \frac{B}{\left(d_{c-c}/D_0\right)^3} \tag{5}$$

in which T_0 is the value of T_B at $d_{c\text{-}c} = D_0$, and A and B are free parameters. The values of A and B are shown in Table 1.

As a general trend in Fig. 3a and b, when the inter-particle distance increased, the reduction of T_B value was observed in all samples. These tendencies were in good agreement with those reported earlier [23, 26]. The reduction of T_B value with a growth of the inter-particle distance was reported in detail in the work of Bae et al. [26] for 5- and 7-nm Fe_3O_4 MNPs. Subsequently, Lan et al. also found that when the concentration increased with a decrease in $d_{c\text{-}c}$ value, the T_B value increased because of the growth of the interacting strength [23]. As one can see, the dependence of T_B on $d_{c\text{-}c}$ was well fitted with Eq. (5) for S1 and S2 samples. For S1 and S2 samples, the blocking temperature decreased with insignificant changes in $d_{c\text{-}c}$ and that included large $d_{c\text{-}c}$. Based on Fig. 3 and Table 1, the value of T_B reduced to 67.23, 83.29, and 83.14% for S1 sample at $\sigma = 0$, $\sigma = 0.1$, and $\sigma = 0.2$, respectively. In the same way, the value of T_B reduced to 64.43, 86.10, and 83.81% for S2 sample at $\sigma = 0$, $\sigma = 0.1$, and $\sigma = 0.2$, respectively. In a previous work, Bae et al. indicated that the value of T_B reduced to 88.00 and 93.33% for 5- and 7-nm Fe_3O_4 MNPs, respectively [26]. All results demonstrated that the simple inter-particle interactions model was suitable to describe the relationship between T_B and $d_{c\text{-}c}$. Despite the data of S3 sample (at $\sigma = 0.1$ and $\sigma = 0.2$)

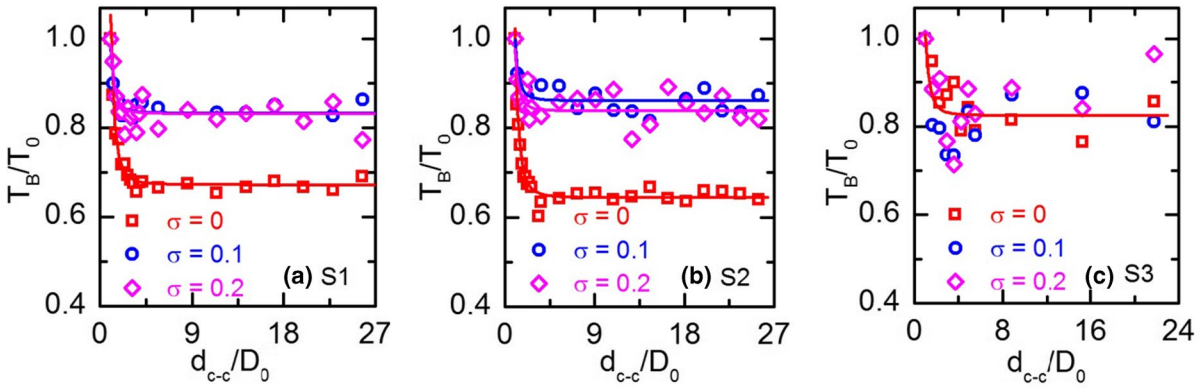

Fig. 3 T_B/T_0 versus $d_{c\text{-}c}/D_0$ with various values of σ for **a** S1, **b** S2, and **c** S3 samples. The solid line represents the fitting curve assuming the theoretical formula: $\frac{T_B}{T_0} = A + \frac{B}{\left(d_{c-c}/D_0\right)^3}$

Table 1 *A* and *B* values for all samples

Sample	*A*			*B*		
	σ = 0	σ = 0.1	σ = 0.2	σ = 0	σ = 0.1	σ = 0.2
S1	0.67231	0.83291	0.83141	0.38144	0.14579	0.15472
S2	0.64432	0.861	0.8381	0.37935	0.13759	0.138
S3	0.82847	–	–	0.18481	–	–

that cannot be fitted under Eq. (9), the reduction of T_B was also observed. For S3 sample, the value of T_B reduced to 74.65, 68.43, and 66.10% for S3 sample at $\sigma = 0$, $\sigma = 0.1$, and $\sigma = 0.2$, respectively. All results indicated that the reduction of T_B occurred when the inter-particle distance increased.

Generally, it is clear that there was a proportional relationship between KV and k_bT_B in practice. So, with a certain value of nanoparticles, the value of magnetic anisotropy will decrease with a fall in T_B. Hence, when the inter-particle distance increased, the strength of inter-particle interaction went down, which could lead to the reduction of T_B and K of MNPs. So, the dipolar interactions among Fe_3O_4 MNPs play an important role in magnetic properties, especially in their value of magnetic anisotropy. It was noted that the K dependence on concentration is used in the calculation of SAR versus K in the following.

When the concentration of MNPs in fluid increased, an increase in the inter-particle interaction could lead to a rising in the value of K of MNPs in the fluid. Thus, the highest value of K of MNPs in fluid might equal the K value of the corresponding dried sample (mentioned in the "Experimental results and discussion" section). Figure 4 presents the plot of SAR versus $K/K_{\text{dried sample}}$ for all samples. From Fig. 4, there was a peak of the plot SAR versus K/K dried sample for S2 and S3 samples. For S1 sample, an increase in SAR value along with K was observed. These results were interesting, which explain previous contradictory results [17–21]. When the concentration went up (related to the inter-particle distance decreased), a growth in the strength of inter-particle interactions lead to an increase in the K value of MNPs. Depending on its size, results from rising K value cause the change (increase or decrease) in SAR value.

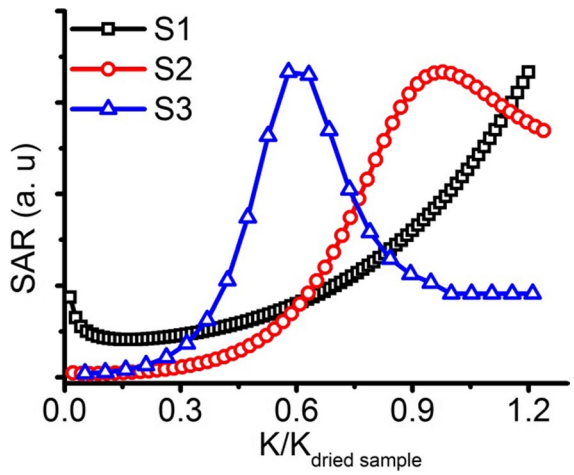

Fig. 4 SAR value versus $K/K_{\text{dried sample}}$ for all samples

Fabrication and experimental results

Fabrication

Chemical

All chemicals used in this work were purchased Sigma-Aldrich Company including iron(II) chloride tetrahydrate ($FeCl_2{\cdot}4H_2O$, ≥ 99%), iron(III) chloride hexahydrate ($FeCl_3{\cdot}6H_2O$, ≥ 99%), and sodium hydroxide (NaOH, ≥ 97%). Deionized water was used in all experiments.

Synthesis of Fe_3O_4 MNPs

Fe_3O_4 MNPs were synthesized by co-precipitation method with the process as follows: dissolve 0.16 g NaOH in 50 ml deionized water. Next, dissolve 0.78 g $FeCl_2{\cdot}4H_2O$ and 2.16 g $FeCl_3{\cdot}6H_2O$ in 50 ml of deionized water. Subsequently, dissolve this solution in the above solution of NaOH. The mixture was stirred at 500 rpm and kept at different temperatures—50, 70, and 90 °C—for 1 h. After that, the

reaction mixture was naturally cooled to room temperature. Using a magnet to collect the black precipitate, wash it with deionized water. The final product of Fe_3O_4 MNPs was collected by a magnet. These products prepared at 50, 70, and 90 °C were denoted as S1, S2, and S3, respectively.

Characterization techniques

The crystalline structures of dried Fe_3O_4 MNPs were analyzed by X-ray diffraction (XRD) (Bruker D8-Advance instrument), in the reflection mode a Cu-Kα line of 1.5406 Å. The morphology of all samples was examined using transmission electron microscopy (TEM) with a TEM system (JEOL JEM-1010). The DC magnetic properties of the samples at room temperature were investigated using a home-made vibrating sample magnetometer under the magnetic field up to 11 kOe. Based on the experimental data of Fe_3O_4 MNPs (size distribution, magnetic saturation), we used MC simulations to investigate the dependence of magnetic anisotropy on the concentration of MNPs. The magnetic induction heating rates of the samples were measured using a commercially available UHF-20A, supplied by Chengdu JinKeZhi Electronic Co, Ltd, at the frequency of 450 kHz and amplitude of 200 Oe. The value of *SAR* was calculated using the following equation [29]:

$$SAR(\mathrm{W/g}) = \frac{C}{m}\frac{\mathrm{d}T}{\mathrm{d}t} \tag{6}$$

where m is the concentration (mg/ml) of sample in magnetic fluid, C is the specific heat capacity of water (4.185 J/gK), and $\mathrm{d}T/\mathrm{d}t$ is the slope of the measured temperature–time curve. In the current experiments, the temperature slope was calculated via analyzing the temperature versus time curves for the whole time range, i.e., first to fit experimental curves by the following equation [30]:

$$T = T_p + \Delta T\left(1 - e^{t/t_m}\right) \tag{7}$$

to gain: ΔT, t_m are the temperature difference between the initial and steady state, and the time constant of heating, respectively.

Then, the value of $\mathrm{d}T/\mathrm{d}t$ is determined as equal to $\Delta T/t_{\mathrm{m}}$. The results from these measurements will be detailed in the results and discussion sections.

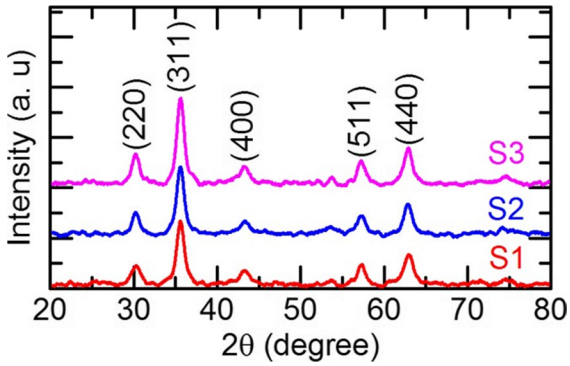

Fig. 5 XRD patterns of S1, S2, and S3 samples

Table 2 $\overline{D_{XRD}}$, D_{311}, $D_{H\text{-}W}$, and D_{TEM} values of all samples

Samples	$\overline{D_{XRD}}$(nm)	D_{311} (nm)	$D_{H\text{-}W}$ (nm)	D_{TEM} (nm)
S1	6.2 ± 1.2	6.8 ± 1.3	5.7 ± 1.1	7.0 ± 1.1
S2	6.6 ± 1.4	6.9 ± 1.0	7.7 ± 1.8	11.0 ± 2.1
S3	6.8 ± 1.5	7 ± 1.1	7.9 ± 1.3	17.0 ± 1.5

Experimental results and discussion

All XRD patterns of S1, S2, and S3 samples are depicted in Fig. 5. A single phase for Fe_3O_4 (MNPs all samples) was confirmed by the reflections indexed as (220), (311), (400), (511), and (440) planes (magnetite, JCPDS card no. 85–1436). Next, we used Scherer's equation to calculate the crystallite size of all samples. The values of D_{311} and $\overline{D_{XRD}}$ were the crystallite size using the profile of the (311) plane and the average crystallite size using all planes, respectively. These obtained values are listed in Table 2.

In addition, we also used the Halder–Wagner method to calculate the samples' crystallite sizes [31, 32]. By this method, the crystallite size, $D_{H\text{-}W}$, was determined by the following equation [31, 32]:

$$\left(\frac{\beta^*}{d^*}\right)^2 = \frac{1}{D_{H-W}}\frac{\beta^*}{(d^*)^2} + \left(\frac{\varepsilon}{2}\right)^2 \tag{8}$$

where $d^* = 2\sin\theta/\lambda$ and $\beta^* = FWHM\cos\theta/\lambda$; ε is the strain, θ is the diffraction angle, *FWHM* is full-width at half maximum of peaks, and λ is the wavelength used.

Following the method mentioned above, the slope of the plot $\left(\frac{\beta^*}{d^*}\right)^2$ verus $\frac{\beta^*}{(d^*)^2}$ (Fig. 6) gave the values of

$D_{H\text{-}W}$ (Table 2). As can be seen in Table 2, all $\overline{D_{XRD}}$, D_{311}, and $D_{H\text{-}W}$ values for S1, S2, and S3 samples are ranging from 6 to 8 nm. The crystallite size of Fe_3O_4 MNPs increases with an increase in reaction temperature. Figure 7a–c present the TEM images of Fe_3O_4 MNPs. The average nanoparticle sizes determined from these TEM images were 7, 11, and 17 nm for S1, S2, and S3 samples, respectively. The solid lines for S1, S2, and S3 samples (Fig. 7d–f) were a good fit for data using the lognormal distribution (Eq. (2)) [5, 29]. All samples had size distribution with $\sigma = 0.1$–0.2.

Next, Fig. 8 shows the typical room temperature (~295 K) magnetic curves for S1, S2, and S3 samples. The obtained magnetization saturation (M_S) was 65.1, 67.0, and 68.1 emu/g corresponding to S1, S2, and S3 samples, respectively. All of them were less than 90 emu/g, their bulk value [22]. Here, there was a surge increase in M_S values with an increase in diameter. This tendency was well suited to those reported earlier [33, 34]. An increase in M_S value of Fe_3O_4 MNPs was found in the work of Goya et al. when its size increased from 5 to 150 nm [33]. This extension could be explained by a core–shell model. Thanks to this model, MNPs might be divided into two parts, including a core of MNPs with the same magnetic properties as their bulk counterpart and a non-magnetic shell. On the other hand, as the nanoparticle size improved, it has a fall in the ratio of surface area to volume leading to an increase in M_S value [34].

$$D_{cr}^{SPM} = \left(\frac{6}{\pi}\frac{25k_BT}{K_{\text{bulk}}}\right)^{1/3} \tag{9}$$

where $K_{\text{bulk}} = 9 \times 10^3$ J/m^3. The obtained D_{cr}^{SPM} value was about 28 nm, whereas our Fe_3O_4 MNPs had size in a range of 7–17 nm. Thus, the superparamagnetic behavior was confirmed for S1, S2, and S3 samples.

In order to determine the value of K for each sample, we fitted data of initial magnetization curves under "the law of approach to saturation" (Fig. 8b) by the following equation [37]:

$$M(H) = M_s\left(1 - \frac{a}{H} - \frac{b}{H^2} - \dots\right) + \chi_p H \tag{10}$$

in which χ_p is the high field differential susceptibility and a, b is free parameter. Subsequently, the value of K can be determined from b by the following equation [37]:

$$b = \frac{4K_{eff}^2}{15M_S^2} \tag{11}$$

The obtained K values were 69.7, 45.9, and 18.7 kJ/m^3 corresponding to samples S1, S2, and S3, respectively. These values were higher than the bulk value (9 kJ/m^3). It was clear that the value of K for Fe_3O_4 decreased from 69.7 to 18.7 kJ/m^3 when size increased from 7 to 17 nm. The main cause of this phenomenon is associated with an increase in the contribution from the surface when the size of MNPs

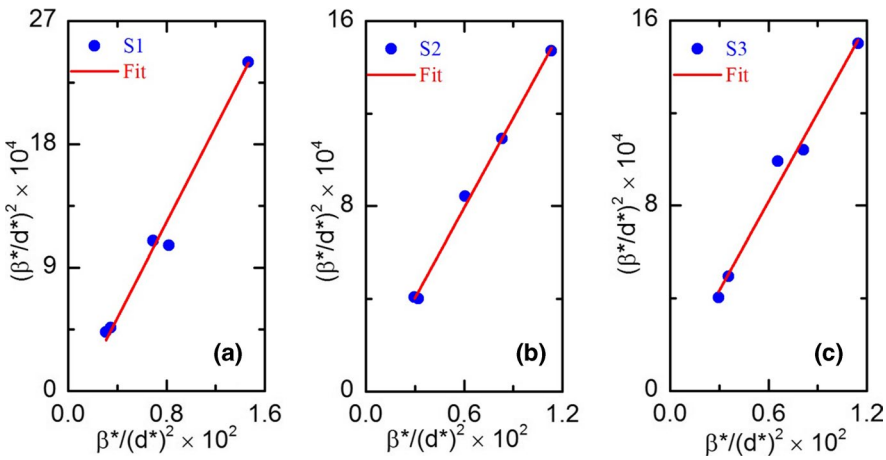

Fig. 6 $\left(\frac{\beta^*}{d^*}\right)^2$ versus $\frac{\beta^*}{(d^*)^2}$ for **a** S1, **b** S2, and **c** S3 samples

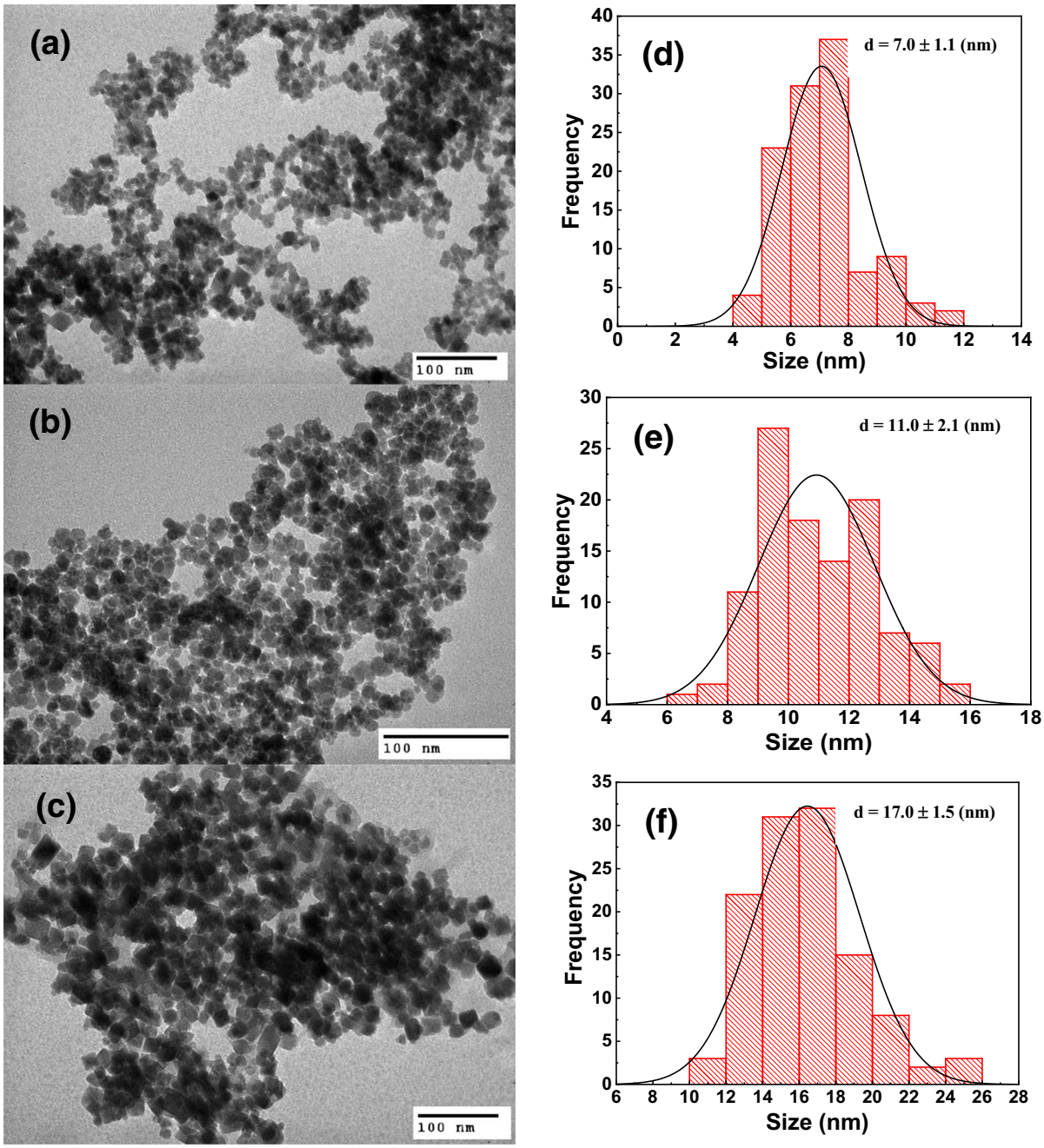

Fig. 7 TEM images and size distribution for **a**–**d** S1, **b**–**e** S2, and **c**–**f** S3 samples

went down. This tendency was compatible with previous theoretical predictions and models [37, 38].

For comparing the theoretical results, the magnetic induction heating rates of the samples at various concentrations were measured (Fig. 9). The value of SAR_{exp} was calculated using Eqs. (6) and (7). Table 3 and Fig. 10 present the value of SAR_{exp} for all samples.

As mentioned in "Theoretical results" section, the K value of each sample increased with an increase of concentration of MNPs. Therefore, we could compare the experimental tendency (Fig. 10) to the theoretical

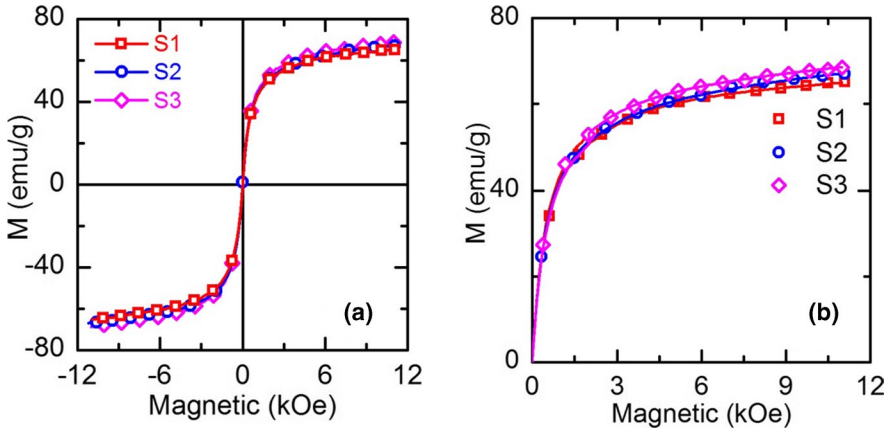

Fig. 8 **a** M–H curves and **b** the initial magnetization curves of Fe_3O_4 MNPs. The solid lines in (**b**) represent the fitting curve assuming "the law of approach to saturation" for all samples. As observed in Fig. 8, all samples had superparamagnetic behavior. In order to confirm this behavior, we used the following equation [35, 36] to calculate the value of critical diameter (D_{cr}^{SPM}) of Fe_3O_4 MNPs and compared it with the D_{TEM} values of all samples.

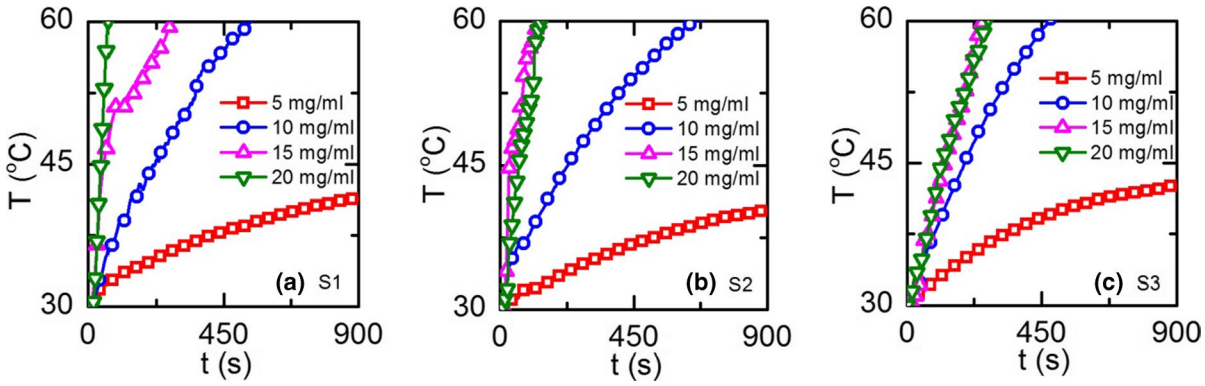

Fig. 9 Magnetic heating curves measured for **a** S1, **b** S2, and **c** S3 samples

Table 3 SAR_{exp} values for S1, S2, and S3 samples

Concentration (mg/ml)	SAR_{exp} (W/g)		
	S1	S2	S3
5	24	22	26
10	39	30	44
15	51	53	48
20	97	65	28

ones (Fig. 4) because the direction of the *x*-axis ($K/K_{dried\ sample}$) in Fig. 4 was similar to itself (concentration) in Fig. 10. For S1 sample, the value of SAR_{exp} increased from 29 to 97 W/g when the concentration of Fe_3O_4 MNPs increased from 5 to 20 mg/ml (Table 3 and Fig. 10). This tendency of S1 sample was compatible with the theoretical prediction in Fig. 4 (as presented in Fig. 10b). For S2 sample, although the theoretical results demonstrated that there was an optimal value of *K*, our experimental results of SAR on *K* might be on the left of the plot of SAR_{theo} versus $K/K_{dried\ sample}$. Similar to S1 sample, the result of S2 sample was in agreement with the theoretical results (as can be seen in Figs. 4 and 10b and Table 3). This tendency of S1 and S2 samples was in agreement with the work of Maternez-Boubeta et al. [19]. In contrast, a decrease in the SAR value while the concentration of MNPs increased was found in ref. [17, 18]. This trend might be on the right of the plot of SAR_{theo} versus $K/K_{dried\ sample}$ for S3 sample (Figs. 4

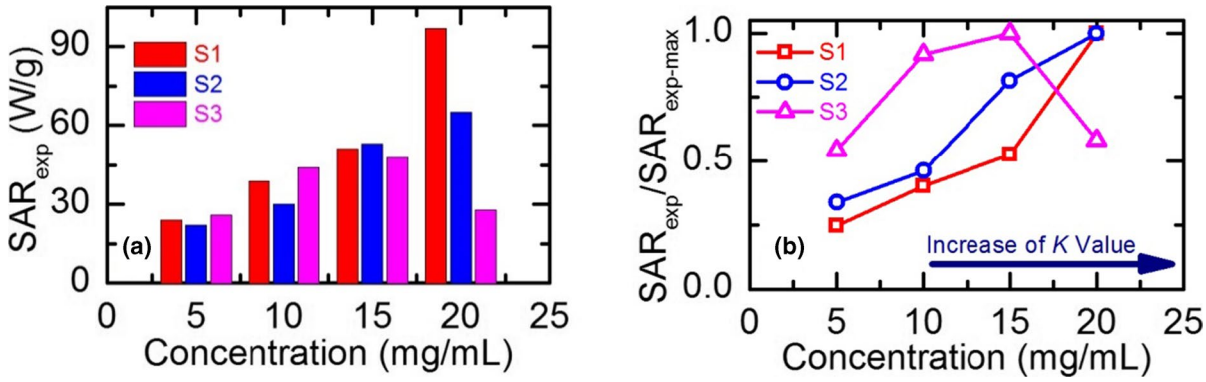

Fig. 10 **a** SAR_{exp} and **b** $SAR_{exp}/SAR_{exp\text{-}max}$ versus concentration for all samples

and 10). Especially, Fig. 10b showed the existence of optimal concentration (at 15 mg/ml) for S3 sample. This experimental result confirmed not only our theoretical predictions (Fig. 7) but also the results of the works of Haase et al. [20] and Kim et al. [21]. In addition, Tan et al. demonstrated that the plot of SAR versus concentration can increase, decrease, or have a bell shape [16], which was in agreement with all of our results. Thus, both theoretical prediction and our experimental results on Fe_3O_4 MNPs indicated that the different influence of the concentration on SAR was caused by its size and its magnetic anisotropy. The Fe_3O_4 MNPs would achieve an optimal concentration when their size was in the range of 11–17 nm.

Conclusion

In summary, the detailed study of MC simulations under the various inter-particle distance suggested that the value of magnetic anisotropy of MNPs increased with an increase in concentration. Nevertheless, it could lead to an increase or decrease in the value of SAR depending on the MNPs' size. Both calculation and experimental study of *SAR* for S1, S2, and S3 samples recognized the important role of magnetic anisotropy to enhance SAR values. In addition, the theoretical results indicated that there is a peak of the plot SAR versus magnetic anisotropy for S2 and S3 samples. Thus, in any case, there was an optimal concentration for 11–17 nm Fe_3O_4 MNPs. Interestingly, our experimental results have shown that SAR_{exp} had the highest value at 15 mg/ml for S3 sample. These outcomes contribute valuable information for the enhancement of SAR for biomedical applications.

Acknowledgements L. T. Dat. is thankful to Dr. Nguyen Duy Vy for fruitful discussions. L. H. Nguyen is thankful to Van Lang University. P. H. Nam is grateful to Institute of Materials Science, Vietnam Academy of Science and Technology (VAST). Fruitful discussions with Dr. Le Dai Nam are warmly acknowledged.

Declarations

Conflict of interest The authors declare that they have no conflict of interest.

References

1. Farzin A., Etesami S. A., Quint J., Memic A., and Tamayol A. (2020) Magnetic nanoparticles in cancer therapy and diagnosis. Adv. Healthcare Mater. 9:1901058(29). https://doi.org/10.1002/adhm.201901058.
2. Kefeni K. K., Msagati T. A. M., Nkambule T. TI., and Mamba B. B. (2020) Spinel ferrite nanoparticles and nanocomposites for biomedical applications and their toxicity. Mater. Sci. Eng. C 107:110314(19). https://doi.org/10.1016/j.msec.2019.110314.
3. Obaidat IM, Issa B, Haik Y (2015) Magnetic properties of magnetic nanoparticles for efficient hyperthermia. Nanomaterials 5:63–89. https://doi.org/10.3390/nano5010063
4. Tong S, Quinto CA, Zhang L, Mohindra P, Bao G (2017) Size-dependent heating of magnetic iron oxide nanoparticles. ACS Nano 11:6808–6816. https://doi.org/10.1021/acsnano.7b01762
5. Rosensweig RE (2002) Heating magnetic fluid with alternating magnetic field. J Magn Magn Mater 252:370–374. https://doi.org/10.1016/S0304-8853(02)00706-0
6. Hergt R., Dutz S., and Röder M. (2008) Effects of size distribution on hysteresis losses of magnetic nanoparticles for

hyperthermia. J. Condens. Matter Phys. 20:385214(12). https://doi.org/10.1088/0953-8984/20/38/385214.
7. Carrey J, Mehdaoui B, Respaud M (2011) Simple models for dynamic hysteresis loop calculations of magnetic single-domain nanoparticles: application to magnetic hyperthermia optimization. J Appl Phys 109:083921-1–083921-17. https://doi.org/10.1063/1.3551582
8. Papadopoulos C, Kolokithas-Ntoukas A, Moreno R, Fuentes D, Loudos G, Loukopoulos VC, Kagadis GC (2022) Using kinetic Monte Carlo simulations to design efficient magnetic nanoparticles for clinical hyperthermia. Med Phys 49:547–567. https://doi.org/10.1002/mp.15317
9. S Eddahri A Razouk M Sajieddine M Sahlaoui 2022 Hysteresis loops on small nanoparticles ferrite spinel by Monte Carlo simulations J Supercond Nov Magn 1–10https://doi.org/10.1007/s10948-022-06242-4
10. Kanaoujiya R, Saroj S. K, Srivastava S, and Chaudhary M. K. (2022) Renewable polysaccharide and biomedical application of nanomaterials. J. Nanomater. https://doi.org/10.1155/2022/1050211
11. Wu Z, Fan F, Yan J, Chen H, Hu X, Su M (2022) An adaptable direct simulation Monte Carlo method for simulating acoustic agglomeration of solid particles. Chem Eng Sci 249:117298. https://doi.org/10.1016/j.ces.2021.117298
12. Binder K, Rauch H, Wildpaner V (1970) Monte Carlo calculation of the magnetization of superparamagnetic particles. J Phys Chem Solids 31:391–397. https://doi.org/10.1016/0022-3697(70)90119-8
13. Binder K. and Stauffer D. (1987) A simple introduction to Monte Carlo simulation and some specialized topics. In: Binder K. (ed) Applications of the Monte Carlo method in statistical physics, 1st edn. Springer Science & Business Media, Berlin, Heidelberg, pp.1–36.
14. Arantes FR, Cornejo DR (2013) Monte Carlo study of the magnetic properties of frozen and non-interacting nanoparticles. J Nanoparticle Res 15:1–10. https://doi.org/10.1007/s11051-013-1859-z
15. Kroese DP, Brereton T, Taimre T, Botev ZI (2014) Why the Monte Carlo method is so important today. Wiley Interdiscip Rev Comput Stat 6:386–392. https://doi.org/10.1002/wics.1314
16. Tan R. P., Carrey J., and Respaud M. (2014) Magnetic hyperthermia properties of nanoparticles inside lysosomes using kinetic Monte Carlo simulations: influence of key parameters and dipolar interactions, and evidence for strong spatial variation of heating power. Phys. Rev. B 90:214421–1–214421–1–12. https://doi.org/10.1103/PhysRevB.90.214421.
17. Urtizberea A, Natividad E, Arizaga A, Castro M, Mediano A (2010) Specific absorption rates and magnetic properties of ferrofluids with interaction effects at low concentrations. J Phys Chem C 114:4916–4922. https://doi.org/10.1021/jp912076f
18. De la Presa P, Luengo Y, Multigner M, Costo R, Morales MP, Rivero G, Hernando A (2012) Study of heating efficiency as a function of concentration, size, and applied field in γ-Fe_2O_3 nanoparticles. J Phys Chem C 116:25602–25610. https://doi.org/10.1021/jp310771p
19. Martinez-Boubeta C, Simeonidis K, Makridis A, Angelakeris M, Iglesias O, Guardia P, Cabot A, Yedra L, Estradé S, Peiró F (2013) Learning from nature to improve the heat generation of iron-oxide nanoparticles for magnetic hyperthermia applications. Sci Rep 3:1–8. https://doi.org/10.1038/srep01652
20. Haase C, Nowak U (2012) Role of dipole-dipole interactions for hyperthermia heating of magnetic nanoparticle ensembles. Phys Rev B 85:045435-1–045435-5. https://doi.org/10.1103/PhysRevB.85.045435
21. Kim J-W, Wang J, Kim H, Bae S (2021) Concentration-dependent oscillation of specific loss power in magnetic nanofluid hyperthermia. Sci Rep 11:1–10. https://doi.org/10.1038/s41598-020-79871-1
22. Phong PT, Nguyen LH, Lee I-J, Phuc NX (2017) Computer simulations of contributions of Néel and Brown relaxation to specific loss power of magnetic fluids in hyperthermia. J Electron Mater 46:2393–2405. https://doi.org/10.1007/s11664-017-5302-6
23. Lan TN, Hai TH (2010) Monte Carlo simulation of magnetic nanoparticle systems. Comput Mater Sci 49:S287–S290. https://doi.org/10.1016/j.commatsci.2010.01.025
24. Nemati Z, Alonso J, Martinez LM, Khurshid H, Garaio E, Garcia JA, Phan MH, Srikanth H (2016) Enhanced magnetic hyperthermia in iron oxide nano-octopods: size and anisotropy effects. J Phys Chem C 120:8370–8379. https://doi.org/10.1021/acs.jpcc.6b01426
25. Habib A. H, Ondeck C. L, Chaudhary P, Bockstaller M. R, and McHenry M. E. (2008) Evaluation of iron-cobalt/ferrite core-shell nanoparticles for cancer thermotherapy. J. Appl. Phys. 103:07A307–1–07A307–3. https://doi.org/10.1063/1.2830975.
26. Bae C. J, Angappane S, Park J.-G, Lee Y, Lee J, An K, and Hyeon T. (2007) Experimental studies of strong dipolar interparticle interaction in monodisperse Fe_3O_4 nanoparticles. Appl. Phys. Lett. 91:102502(3). https://doi.org/10.1063/1.2778758.
27. Deatsch AE, Evans BA (2014) Heating efficiency in magnetic nanoparticle hyperthermia. J Magn Magn Mater 354:163–172. https://doi.org/10.1016/j.jmmm.2013.11.006
28. García-Otero J, Porto M, Rivas J, Bunde A (2000) Influence of dipolar interaction on magnetic properties of ultrafine ferromagnetic particles. Phys Rev Lett 84:167–170. https://doi.org/10.1103/PhysRevLett.84.167
29. Nguyen LH, Phuc NX, Manh DH, Nam NH, Truong NX, Quynh NV, Phong PT, Nam PH (2021) Size-dependent magnetic heating of $MnFe_2O_4$ nanoparticles. J Electron Mater 50:5318–5326. https://doi.org/10.1007/s11664-021-09056-7
30. Bekovic M. and Hamler A. (2010) Determination of the heating effect of magnetic fluid in alternating magnetic field. IEEE Trans. Magn. 46:552–555. https://doi.org/10.1109/TMAG.2009.2033944
31. Radoń A, Hawełek Ł, Łukowiec D, Kubacki J, Włodarczyk P (2019) Dielectric and electromagnetic interference shielding properties of high entropy (Zn, Fe, Ni, Mg, Cd) Fe_2O_4 ferrite. Sci Rep 9:1–13. https://doi.org/10.1038/s41598-019-56586-
32. Patel CM, Chakraborty M, Murthy ZVP (2014) Study on the stability and microstructural properties of barium sulfate nanoparticles produced by nanomilling. Adv Powder

Technol 25:226–235. https://doi.org/10.1016/j.apt.2013.04.003
33. Goya GF, Berquo TS, Fonseca FC, Morales MP (2003) Static and dynamic magnetic properties of spherical magnetite nanoparticles. J Appl Phys 94:3520–3528. https://doi.org/10.1063/1.1599959
34. Iglesias O. and Labarta A. (2001) Finite-size and surface effects in maghemite nanoparticles: Monte Carlo simulations. Phys. Rev. B. 63:184416(18). https://doi.org/10.1103/PhysRevB.63.184416
35. Phong PT, Nguyen LH, Phong LTH, Nam PH, Manh DH, Lee I-J, Phuc NX (2017) Study of specific loss power of magnetic fluids with various viscosities. J Magn Magn Mater 428:36–42. https://doi.org/10.1016/j.jmmm.2016.12.008
36. Rafique MY, Li-Qing P, Iqbal MZ, Hong-Mei Q, Farooq MH, Zhen-Gang G, Tanveer M (2013) Growth of monodisperse nanospheres of $MnFe_2O_4$ with enhanced magnetic and optical properties. Chin Phys B 22:107101-1–107101-7. https://doi.org/10.1088/1674-1056/22/10/107101
37. Nguyen L. H, Oanh V. T. K, Nam P. H, Doan D. H, Truong N. X, Ca N. X, Phong P. T, Hong L. V, and Lam T. D. (2020) Increase of magnetic hyperthermia efficiency due to optimal size of particles: theoretical and experimental results. J. Nanopart. Res. 22:258(16). https://doi.org/10.1007/s11051-020-04986-5
38. Yanes R., Chubykalo-Fesenko O., Kachkachi H., Garanin D. A., Evans R., and Chantrell R. W. (2007) Effective anisotropies and energy barriers of magnetic nanoparticles with Néel surface anisotropy. 76:064416(6). https://doi.org/10.1103/PhysRevB.76.064416